Spatially Coupled Hybrid Concatenated Codes

Spatially Coupled Hybrid Concatenated Codes

Saeedeh Moloudi†, Michael Lentmaier†, and Alexandre Graell i Amat‡
†Department of Electrical and Information Technology, Lund University, Lund, Sweden
‡Department of Signals and Systems, Chalmers University of Technology, Gothenburg, Sweden
{saeedeh.moloudi,michael.lentmaier}@eit.lth.se, alexandre.graell@chalmers.se

***Abstract*—The main purpose of this paper is to make the study of spatially coupled turbo-like codes (SC-TCs) more complete by investigating the impact of spatial coupling on the thresholds of hybrid concatenated codes (HCCs). In our previous studies, we introduced some classes of SC-TCs and considered their density evolution (DE) analysis. The obtained results indicated that for a fixed coupling memory, braided convolutional codes (BCCs) yield the best belief propagation (BP) thresholds among the considered classes. Besides having excellent BP thresholds, BCCs have good distance properties and their minimum distance grows linearly with the block length. Similarities between BCCs and HCCs make HCCs good competitors for BCCs. This has motivated us to investigate the impact of spatial coupling on HCCs. In this paper, we introduce two spatially coupled ensembles of HCCs, referred to as Type-I SC-HCCs and Type-II SC-HCCs. Then, we derive the exact density evolution equations for the uncoupled and the coupled ensembles for the binary erasure channel. Finally, considering different component encoders, we compute the thresholds of the SC-HCC ensembles and compare them with the thresholds of BCCs for a range of different rates.**

I. Introduction

In the last years, there has been a growing interest in low-density parity-check (LDPC) convolutional codes [1], also known as spatially coupled LDPC (SC-LDPC) codes [2]. These codes exhibit a remarkable behavior called threshold saturation; for them, the belief propagation (BP) decoder can achieve the threshold of the optimal maximum-a-posteriori (MAP) decoder.

Spatial coupling is a general concept that is not limited to LDPC codes. Spatially coupled turbo-like codes (SC-TCs) were introduced in [3], [4]. In these articles, various ensembles of spatially coupled parallel and serially concatenated codes (SC-PCCs and SC-SCCs) were proposed. Moreover, two extensions of braided convolutional codes (BCCs) for higher coupling memory were introduced, referred to as Type-I BCCs and Type-II BCCs. For the binary erasure channel (BEC), the exact density evolution (DE) equations of the considered SC-TCs were derived and the BP thresholds of the coupled ensembles were obtained. The numerical results in [4] indicate improvements in the BP thresholds of the coupled ensembles and the occurrence of threshold saturation. Threshold saturation was proved analytically for SC-TCs over the BEC in [4], [5].

The DE analysis of SC-TCs shows that the Type-II BCC ensemble has the best BP threshold among the considered SC-TC ensembles. On the other hand, the finite block length analysis of BCCs in [6] indicates that the minimum distance of BCCs grows linearly with the permutation size. It is also shown that for BCCs very low error rates can be achieved by avoiding a small fraction of bad permutations. Having close-to-capacity thresholds and very low error floor, makes BCCs a very promising class of codes.

Hybrid concatenated codes (HCCs) [7], [8] are a class of turbo-like codes which are closely related to BCCs. Similar to the BCC ensemble, the HCC ensemble is a mixture of parallel and serially concatenated code ensembles. Also for HCCs, the minimum distance grows linearly with the permutation size. In addition, they can achieve very low error rates in the error floor region [7], [8]. The remarkable properties of HCCs and their similarities with BCCs, have motivated us to investigate the impact of spatial coupling on HCCs.

As a first step, we briefly review SC-TCs. Then, we propose two ensembles of spatially coupled HCCs (SC-HCCs), referred to as Type-I SC-HCCs and Type-II SC-HCCs. We also derive the exact DE equations for the proposed ensembles and compute the thresholds of BP decoding for the BEC. Furthermore, using the area theorem we compute the MAP threshold. We also consider different component encoders to investigate the impact of the component encoders on the decoding thresholds of SC-HCCs. By considering random puncturing, we perform a threshold analysis for a family of rate compatible SC-HCCs. Finally, we compare the obtained numerical results with the corresponding results for BCCs.

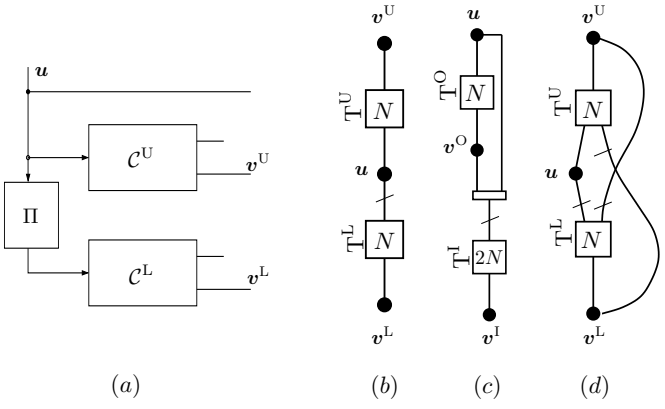

Fig. 1. (a) Block diagram of PCCs. Compact graph representation of (b) PCCs, (c) SCCs and (d) BCCs.

This work was supported in part by the Swedish Research Council (VR) under grant #621-2013-5477.

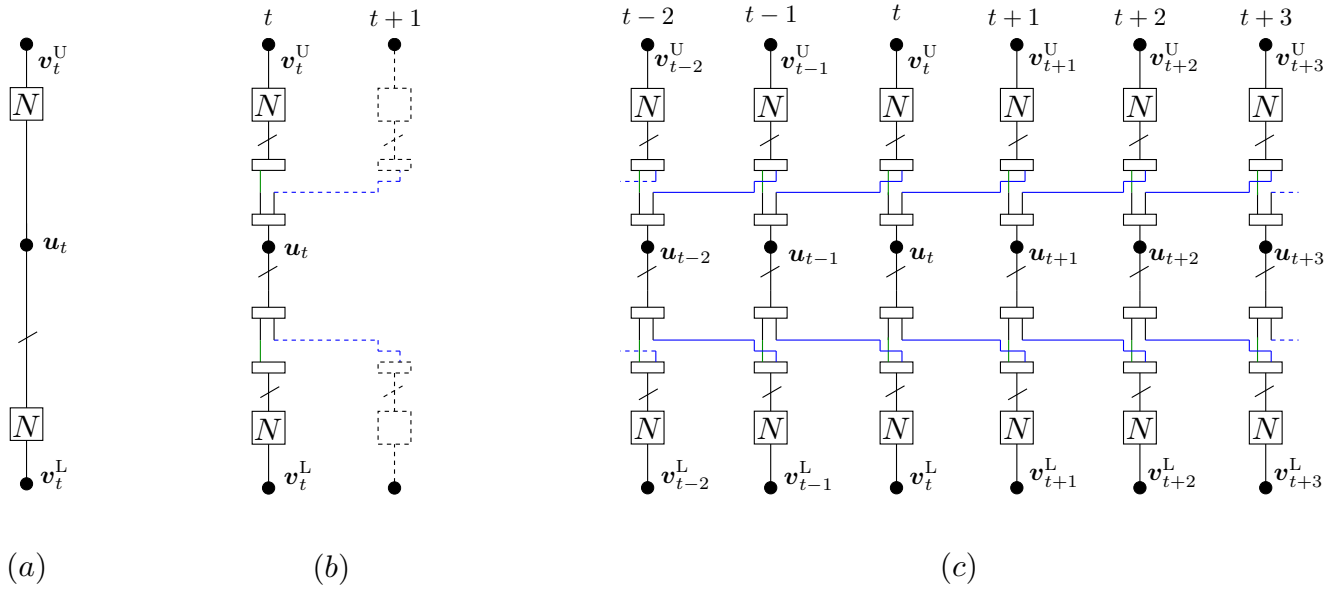

Fig. 2. Compact graph representation (a) PCC (b) SC-PCC at time instant t (c) SC-PCC.

II. Spatially Coupled Turbo-like Codes

A. Compact Graph Representation

In our previous studies [4], we considered three main classes of TCs; including PCCs, SCCs, and BCCs. The compact graph representation of these codes is shown in Fig. 1. This new representation makes the illustration of TCs and SC-TCs simpler, and makes the DE analysis of theses codes more convenient. In this graph representation, the variable nodes, corresponding to information and parity sequences, are shown by black circles, and the factor nodes corresponding to the component trellises are represented by squares. These factor nodes are also labeled by the length of the corresponding trellises.

As an example, the block diagram of the PCC encoder and the compact graph of PCCs are shown in Fig. 1 (a) and (b), respectively. In the compact graph representation, the information sequence $\boldsymbol{u}$ is connected to the upper trellis T^{U} to produce the upper parity sequence $\boldsymbol{v}^{\mathrm{U}}$. Likewise, a reorded copy of $\boldsymbol{u}$ is connected to the lower trellis T^{L} to produce the lower parity sequence $\boldsymbol{v}^{\mathrm{L}}$. To illustrate that a reordered copy of $\boldsymbol{u}$ is connected to T^{L}, the corresponding permutation is shown by a cross line on the edge which connects $\boldsymbol{u}$ to T^{L}.

Consider the PCC ensemble at time t in Fig. 2 (a). In order to obtain the coupled ensemble —as it is shown in Fig. 2 (b)— the information sequence, $\boldsymbol{u}_t$, is divided into two sequences of equal size, $\boldsymbol{u}_{t,0}$ and $\boldsymbol{u}_{t,1}$, by a multiplexer (the multiplexer is illustrated by a rectangle in the graph). Then, the sequence $\boldsymbol{u}_{t,0}$ is used as a part of the input to the upper encoder at time t and $\boldsymbol{u}_{t,1}$ is used as a part of the input to the upper encoder at time $t+1$. Likewise, a reordered copy of the information sequence, $\tilde{\boldsymbol{u}}_t$, is divided into two sequences $\tilde{\boldsymbol{u}}_{t,0}$ and $\tilde{\boldsymbol{u}}_{t,1}$. These sequences are connected to the lower encoders at time t and $t+1$, respectively.

Consider a collection of L PCCs at time instants $t = 1, ..., L$ (Fig. 2 (c)), where L is called the coupling length. Similarly to Fig. 2 (b), divide the information sequence $\boldsymbol{u}_t$, $t = 1, \ldots, L$, into two sequences $\boldsymbol{u}_{t,0}$ and $\boldsymbol{u}_{t,1}$. The input to the upper encoder at t is a reordered copy of $(\boldsymbol{u}_{t,0}, \boldsymbol{u}_{t-1,1})$. Likewise, the input to the lower encoder at time t is a reordered copy of $(\tilde{\boldsymbol{u}}_{t,0}, \tilde{\boldsymbol{u}}_{t-1,1})$.

In the SC-PCC ensemble in Fig. 2 (c), the coupling memory is equal to $m = 1$ as $\boldsymbol{u}_t$ is used only at the time instants t and $t+1$. It is possible to obtain higher coupling memory m by dividing each of the sequences $\boldsymbol{u}_t$ and $\tilde{\boldsymbol{u}}_t$ into $m+1$ sequences of equal size and spread these sequences respectively to the input of the upper and the lower encoder at time slots t to $t+m$ [4].

Similarly to PCCs, it is possible to apply spatial coupling on SCCs and increase the coupling memory for BCCs. The SC-TC ensemble are described in detail and illustrated in [4].

B. Density Evolution Equations and Decoding Thresholds

Considering transmission over a BEC, we can analyze the asymptotic behavior of TCs and SC-TCs by tracking the evolution of the erasure probability in different iterations of the decoding procedure. This evolution can be shown as a set of equations called DE equations, and for the BEC, it is possible to derive an exact expression for them. By use of the DE equations, we compute the threshold of BP decoding. The BP threshold is the largest channel erasure probability ε for which the erasure probability at the output of the BP decoder converges to zero as the block length and number of iterations go to infinity. The BP thresholds, $\varepsilon_{\mathrm{BP}}$, of the considered TC ensembles are computed and summarized in Table I for rate $R = \frac{1}{3}$.

We also computed the MAP thresholds of the ensembles, $\varepsilon_{\mathrm{MAP}}$, by use of the area theorem [9]. According to the

TABLE I
THRESHOLDS OF PCCS, SCCS AND BCCS WITH $R = \frac{1}{3}$, $m = 1$.

Ensemble	ε_{BP}	ε_{MAP}	ε_{SC}
PCC	0.6428	0.6553	0.6553
SCC	0.5405	0.6654	0.6437
Type-I BCC	0.5541	0.6653	0.6609
Type-II BCC	0.5541	0.6653	0.6651

area theorem, the MAP threshold[1] can be obtained from the following equation

$$\int_{\varepsilon_{\text{MAP}}}^{1} \bar{p}_{\text{extr}}(\varepsilon) d\varepsilon = R \ ,$$

where R is the rate of the code and $\bar{p}_{\text{extr}}(\varepsilon)$ is the average extrinsic erasure probability for all transmitted bits.

According to the values shown for ε_{BP} and ε_{MAP}, while the uncoupled BCC ensembles have the worst BP thresholds, they have very good MAP thresholds. The last column of the table shows the BP thresholds of coupled ensembles with coupling memory $m = 1$. The BP threshold of the Type-II BCC ensemble improves significantly and this coupled ensemble has the best BP threshold for $m = 1$.

III. HYBRID CONCATENATED CODES

In this paper, we consider a rate $R = \frac{1}{5}$ HCC ensemble consisting of a PCC encoder as an outer encoder which is serially concatenated with an inner encoder. The block diagram representation of the HCC encoder is shown in Fig. 3. The outer encoder is built of two rate-1 recursive systematic convolutional (RSC) encoders with N trellis sections, referred to as upper and lower encoders, respectively. The inner encoder is an RSC encoder with $2N$ trellis sections.

The information sequence $\boldsymbol{u}$ is connected to $\mathcal{C}^{\text{U}}$ to produce the upper parity sequence $\boldsymbol{v}^{\text{U}}$. Likewise, a reordered copy of $\boldsymbol{u}$ is connected to $\mathcal{C}^{\text{L}}$ to produce the lower parity sequence $\boldsymbol{v}^{\text{L}}$. Then, the sequences $\boldsymbol{v}^{\text{U}}$ and $\boldsymbol{v}^{\text{L}}$ are multiplexed and properly reordered by permutation Π^{I}. The resulting sequence is used as the input sequence for the inner encoder $\mathcal{C}^{\text{I}}$ to produce the parity sequence $\boldsymbol{v}^{\text{I}}$. Finally, the encoded sequence is $\boldsymbol{v} = (\boldsymbol{u}, \boldsymbol{v}^{\text{U}}, \boldsymbol{v}^{\text{L}}, \boldsymbol{v}^{\text{I}})$.

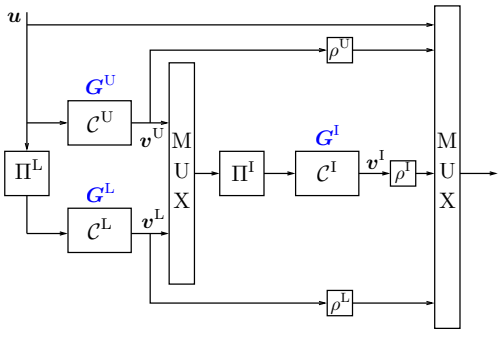

Fig. 3. Block diagram representation of an HCC encoder.

[1]The obtained threshold from the area theorem is an upper bound on the MAP threshold. However, the numerical results show that the threshold of the coupled ensemble converges to this upper bound. This indicates that the upper bound on the MAP threshold is a tight bound.

A family of rate-compatible SC-HCCs can be obtained by applying puncturing. We denote by $\rho \in [0, 1]$ the fraction of surviving bits in a sequence after puncturing, referred to as permeability rate. Consider random puncturing with permeability rates ρ^{U}, ρ^{L} and ρ^{I} for the sequences $\boldsymbol{v}_t^{\text{U}}$, $\boldsymbol{v}_t^{\text{L}}$, and $\boldsymbol{v}_t^{\text{I}}$, respectively. The overall code rate is

$$R = \frac{1}{1 + \rho^{\text{U}} + \rho^{\text{L}} + 2\rho^{\text{I}}}.$$

Fig. 4(a) shows the compact graph representation of the considered HCC ensemble. The factor nodes corresponding to the upper, lower, and inner trellises are represented by squares and denoted by T^{U}, T^{L} and T^{I}, respectively.

The information sequence $\boldsymbol{u}$ is connected to T^{U} to produce the upper parity sequence $\boldsymbol{v}^{\text{U}}$. Likewise, a reordered copy of $\boldsymbol{u}$ is connected to T^{L} to produce $\boldsymbol{v}^{\text{L}}$. Note that in the graph, the permutation Π^{L} is illustrated by the line which crosses the edge between $\boldsymbol{u}$ and T^{L}. The sequences $\boldsymbol{v}^{\text{U}}$ and $\boldsymbol{v}^{\text{L}}$ are multiplexed and properly reordered. The resulting sequence is connected to T^{I} to produce $\boldsymbol{v}^{\text{I}}$.

IV. SPATIALLY COUPLED HYBRID CONCATENATED CODES

A. Type-I Spatially Coupled Hybrid Concatenated Codes

The compact graph representation of the Type-I SC-HCC ensemble with coupling memory m is shown in Fig. 4(b) for time instant t. Consider a collection of L blocks of HCCs at time instants $t = 1, \ldots, L$. The information sequence at time t is denoted by $\boldsymbol{u}_t$. Similarly to uncoupled HCCs, $\boldsymbol{u}_t$ and a reordered copy of $\boldsymbol{u}_t$ are connected to T_t^{U} and T_t^{L} to produce the current parity sequences $\boldsymbol{v}_t^{\text{U}}$ and $\boldsymbol{v}_t^{\text{L}}$, respectively. Then, $\boldsymbol{v}_t^{\text{U}}$ and $\boldsymbol{v}_t^{\text{L}}$ are multiplexed and reordered. The resulting sequence is denoted by $\tilde{\boldsymbol{v}}_t^{\text{O}}$. In order to obtain a coupled ensemble with memory m, $\tilde{\boldsymbol{v}}_t^{\text{O}}$ is divided into $m + 1$ equal-sized sequences, denoted by $\tilde{\boldsymbol{v}}_{t,j}^{\text{O}}$, $j = 0, \ldots, m$. At time t, the input of the inner encoder is a reordered version of $(\tilde{\boldsymbol{v}}_{t,0}^{\text{O}}, \tilde{\boldsymbol{v}}_{t-1,1}^{\text{O}}, \ldots, \tilde{\boldsymbol{v}}_{t-m,m}^{\text{O}})$. The corresponding parity sequence is denoted by $\boldsymbol{v}_t^{\text{I}}$. Finally, the unpunctured code sequence is $\boldsymbol{v}_t = (\boldsymbol{u}_t, \boldsymbol{v}_t^{\text{U}}, \boldsymbol{v}_t^{\text{L}}, \boldsymbol{v}_t^{\text{I}})$.

B. Type-II Spatially Coupled Hybrid Concatenated Codes

Fig. 4(c) depicts the compact graph representation of the Type-II SC-HCC ensemble. This ensemble is equivalent to the Type-I SC-HCC ensemble in most of the parts. For Type-II SC-HCCs, in addition to the coupling of the parity sequences $\boldsymbol{v}_t^{\text{U}}$ and $\boldsymbol{v}_t^{\text{L}}$, we consider the coupling of the information sequence $\boldsymbol{u}_t$. At time t, $\boldsymbol{u}_t$ is divided into $m + 1$ equal-sized sequences $\boldsymbol{u}_{t,j}$, $j = 0, \ldots, m$. Likewise, a reordered copy of the information sequence, $\tilde{\boldsymbol{u}}_t$, is divided into $m + 1$ equal-sized sequences $\tilde{\boldsymbol{u}}_{t,j}$, $j = 0, \ldots, m$. At time t, the sequence $(\boldsymbol{u}_{t-0,0}, \boldsymbol{u}_{t-1,1}, \ldots, \boldsymbol{u}_{t-m,m})$ and a reordered copy of the sequence $(\tilde{\boldsymbol{u}}_{t-0,0}, \tilde{\boldsymbol{u}}_{t-1,1}, \ldots, \tilde{\boldsymbol{u}}_{t-m,m})$ are the input sequences for the upper and the lower encoder, respectively.

V. DENSITY EVOLUTION ANALYSIS ON THE BEC

In this section, we assume transmission over the BEC with erasure probability ε. We derive the exact DE equations for the SC-HCC ensembles with coupling memory m. Note that

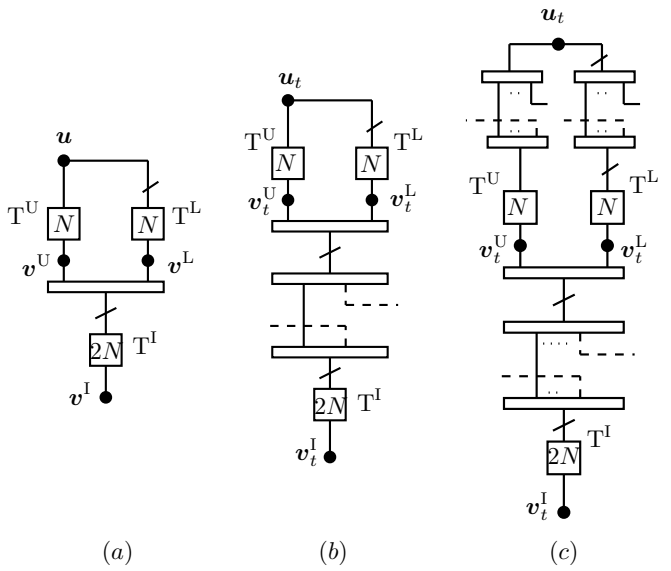

Fig. 4. (a) Compact graph representation of (a) HCC (b) Type-I SC-HCC (c) Type-II SC-HCC.

the DE equations for the uncoupled HCC ensemble can be obtained by considering $m = 0$ and removing the time index in the DE equations of the SC-HCC ensembles. Using the obtained DE equations, we analyze the asymptotic behavior of the ensembles in the next section.

A. Type-I Spatially Coupled Hybrid Concatenated Codes

Consider the Type-I SC-HCC ensemble with coupling memory m in Fig. 4(b). The factor node T^{U} is connected to the variable nodes $\boldsymbol{u}_t$ and $\boldsymbol{v}_t^{\mathrm{U}}$. In the ith iteration, the average extrinsic erasure probabilities from T^{U} to $\boldsymbol{u}_t$ and $\boldsymbol{v}_t^{\mathrm{U}}$ are denoted by $p_{\mathrm{U,s}}^{(i,t)}$ and $p_{\mathrm{U,p}}^{(i,t)}$, respectively. Likewise, $p_{\mathrm{L,s}}^{(i,t)}$ and $p_{\mathrm{L,p}}^{(i,t)}$ denote the average extrinsic erasure probabilities from T^{L} to $\boldsymbol{u}_t$ and $\boldsymbol{v}_t^{\mathrm{L}}$, respectively. Then, the DE updates for T^{U} are

$$p_{\mathrm{U,s}}^{(i,t)} = f_{\mathrm{U,s}}\Big(q_{\mathrm{L}}^{(i-1,t)}, q_{\mathrm{I}}^{(i-1,t)}\Big), \tag{1}$$

$$p_{\mathrm{U,p}}^{(i,t)} = f_{\mathrm{U,p}}\Big(q_{\mathrm{L}}^{(i-1,t)}, q_{\mathrm{I}}^{(i-1,t)}\Big), \tag{2}$$

where

$$q_{\mathrm{L}}^{(i,t)} = \varepsilon \cdot p_{\mathrm{L,s}}^{(i,t)}, \tag{3}$$

$$q_{\mathrm{I}}^{(i,t)} = \varepsilon \cdot \frac{\sum_{j=0}^{m} p_{\mathrm{I,s}}^{(i,t+j)}}{m+1}, \tag{4}$$

and $f_{\mathrm{U,s}}$ and $f_{\mathrm{U,p}}$ are the transfer functions of T^{U} for the systematic and parity bits, respectively. Note that $p_{\mathrm{I,s}}^{(i,t)}$ in (4) denotes the average extrinsic erasure probabilities from T^{I} to the set of $\boldsymbol{v}_{t'}^{\mathrm{U}}$ and $\boldsymbol{v}_{t'}^{\mathrm{L}}$, $t' = t-m, \ldots, t$, which are connected to it. The method proposed in [10] is used to obtain the exact transfer functions of the component decoders.

The DE updates of the lower decoder are identical to those of the upper decoder with the indexes U and L are interchanged.

Similarly, the DE updates of T^{I} can be written as

$$p_{\mathrm{I,s}}^{(i,t)} = f_{\mathrm{I,s}}\Big(q_{\mathrm{UL}}^{(i-1,t)}, \varepsilon\Big), \tag{5}$$

$$p_{\mathrm{I,p}}^{(i,t)} = f_{\mathrm{I,p}}\Big(q_{\mathrm{UL}}^{(i-1,t)}, \varepsilon\Big), \tag{6}$$

where

$$q_{\mathrm{UL}}^{(i,t)} = \varepsilon \cdot \frac{\sum_{k=0}^{m} p_{\mathrm{U,s}}^{(i,t-k)} + p_{\mathrm{L,s}}^{(i,t-k)}}{2(m+1)}, \tag{7}$$

and $f_{\mathrm{I,s}}$ and $f_{\mathrm{I,p}}$ are the transfer functions of T^{I} for the systematic and parity bits, respectively.

Finally, the a-posteriori erasure probability on u_t at time t and iteration i is

$$p_a^{(i,t)} = \varepsilon \cdot p_{\mathrm{U,s}}^{(i,t)} \cdot p_{\mathrm{L,s}}^{(i,t)}. \tag{8}$$

B. Type-II Spatially Coupled Hybrid Concatenated Codes

Consider the Type-II SC-HCC ensemble with coupling memory m in Fig. 4(c). As we discussed in the previous section, this ensemble is identical to the Type-I SC-HCC ensemble except that in the Type-II SC-HCC ensemble the information bits are also coupled. Therefore, the DE updates of the Type-II SC-HCC ensemble are identical to the DE updates of the Type-I SC-HCC ensemble except for (3). According to the compact graph representation in Fig. 4(c), the information variable node $\boldsymbol{u}_t$ is connected to the set of $T_{t''}^{\mathrm{U}}$s at time instants $t'' = t, \ldots, t+m$. The reordered copy of $\boldsymbol{u}_t$ is also connected to the set of $T_{t''}^{\mathrm{L}}$s, $t'' = t, \ldots, t+m$. Thus, (3) is rewritten as

$$q_{\mathrm{L}}^{(i,t)} = \varepsilon \cdot \frac{1}{(m+1)^2} \sum_{k=0}^{m} \sum_{j=0}^{m} p_{\mathrm{L,s}}^{(i,t+j-k)}. \tag{9}$$

Finally, the a-posteriori erasure probability on u_t at time t and iteration i is

$$p_a^{(i,t)} = \frac{q_{\mathrm{U}}^{(i,t)} \cdot q_{\mathrm{L}}^{(i,t)}}{\varepsilon}. \tag{10}$$

C. Random Puncturing

Assume transmission over a BEC with erasure probability ε. Puncturing a sequence with permeability rate ρ is equivalent to transmitting the sequence over a BEC with erasure probability $\varepsilon_\rho = 1 - (1-\varepsilon)\rho$. Thus, we can modify the DE equations of SC-HCCs to account for the random puncturing by considering the corresponding ε_ρs for the transmitted sequences.

As we discussed in the previous section, we denote the permeability rates for the upper, lower, and inner sequence by ρ^{U}, ρ^{L} and ρ^{I}, respectively. The DE updates for the punctured Type-I SC-HCCs are obtained by substituting $\varepsilon_{\rho^{\mathrm{U}}} \leftarrow \varepsilon$ in (4) ($\varepsilon_{\rho^{\mathrm{L}}} \leftarrow \varepsilon$ in the corresponding equation for the lower decoder) and $\varepsilon_{\rho^{\mathrm{I}}} \leftarrow \varepsilon$ in (5) and (6). Moreover, the (7) is modified to

$$q_{\mathrm{UL}}^{(i,t)} = \frac{\sum_{k=0}^{m} \varepsilon_{\rho^{\mathrm{U}}} \cdot p_{\mathrm{U,s}}^{(i,t-k)} + \varepsilon_{\rho^{\mathrm{L}}} \cdot p_{\mathrm{L,s}}^{(i,t-k)}}{2(m+1)}. \tag{11}$$

The DE updates for the punctured Type-II SC-HCC ensemble are identical to those of the punctured Type-I SC-HCC ensemble, except of the modified versions of the equation (3) and its corresponding equation for the lower decoder. For the

TABLE II
GENERATOR MATRICES OF THE COMPONENT ENCODERS

Ensemble	$\boldsymbol{G}^{\mathrm{U}} = \boldsymbol{G}^{\mathrm{L}}$	$\boldsymbol{G}^{\mathrm{I}}$
SC-HCC-I	$(1, 1/3)$	$(1, 5/7)$
SC-HCC-II	$(1, 5/7)$	$(1, 5/7)$
SC-HCC-III	$(1, 5/7)$	$(1, 1/3)$

TABLE III
THRESHOLDS FOR PCCS, SCCS, BCCS AND HCCS WITH $R = \frac{1}{3}$

Ensemble	Type	$\varepsilon_{\mathrm{BP}}$	$\varepsilon_{\mathrm{MAP}}$	$\varepsilon^{1}_{\mathrm{SC}}$
PCC	-	0.6428	0.6553	0.6553
SCC	-	0.5405	0.6654	0.6437
BCC	Type-I	0.5541	0.6653	0.6609
BCC	Type-II	0.5541	0.6653	0.6651
HCC-I	Type-I	0.4961	0.6666	0.6398
HCC-I	Type-II	0.4961	0.6666	0.6611
HCC-II	Type-I	0.3480	0.6666	0.5667
HCC-II	Type-II	0.3480	0.6666	0.6181
HCC-III	Type-I	0.5456	0.6665	0.5943
HCC-III	Type-II	0.5456	0.6665	0.6382

punctured Type-II SC-HCCs, $q_{\mathrm{L}}^{(i,t)}$ is obtained by substituting $\varepsilon_{\rho^{\mathrm{U}}} \leftarrow \varepsilon$ in equation (9). Likewise, $q_{\mathrm{U}}^{(i,t)}$ is obtained by substituting $\varepsilon_{\rho^{\mathrm{L}}} \leftarrow \varepsilon$ in the corresponding for the lower decoder.

VI. RESULTS AND DISCUSSION

In this section, we compute the BP thresholds of HCCs and SC-HCCs by use of the DE equations derived in Section IV. In order to investigate the impact of the component encoders on the thresholds of HCCs, we consider three different cases, referred to as HCC-I, HCC-II and HCC-III. In all cases, we assume identical upper and lower component encoders. The generator matrices of the component encoders are shown in Table II, in octal notation. In this table, the generator matrix of the upper, lower, and inner encoder are denoted by $\boldsymbol{G}^{\mathrm{U}}$, $\boldsymbol{G}^{\mathrm{L}}$ and $\boldsymbol{G}^{\mathrm{I}}$, respectively.

The upper and lower component encoders of HCC-I are considered to be a simple 2-state RSC encoder with generator matrix $\boldsymbol{G} = (1, 1/3)$. The inner component encoder is a 4-state RSC encoders with generator matrix $\boldsymbol{G} = (1, 5/7)$. For HCC-II, we consider three identical RSC encoders for the upper, lower and inner components. These encoders have generator matrix $\boldsymbol{G} = (1, 5/7)$. Finally, for HCC-III, we considered similar component encoders as for HCC-I but with a different order. The upper and lower components are the 2-state RSC encoders, while the inner component is the 4-state RSC encoder. The decoding thresholds are computed for HCC-I, HCC-II and HCC-III and results are summarized in Table III. In order to obtain a code with rate $R = 1/3$, random puncturing is considered with $\rho^{\mathrm{U}} = 0$, $\rho^{\mathrm{L}} = 0$, and $\rho^{\mathrm{I}} = 1$.

According to our numerical results, in general all three considered HCC ensembles suffer from relatively bad BP thresholds and the HCC-II ensemble has the weakest BP threshold. The MAP thresholds, $\varepsilon_{\mathrm{MAP}}$, are almost identical, but that of the HCC-III ensemble is slightly worse. However, the MAP thresholds of all three HCCs are excellent, even better than the MAP thresholds of BCCs and SCCs. In other words, for the HCC ensembles, the gap to the Shannon limit is smaller than that of BCC and SCC ensembles. Applying the coupling results in improved BP thresholds. Similarly to BCCs, Type-II SC-HCC ensembles have better BP thresholds than Type-I SC-HCC ensembles.

As the HCC-II ensemble has the worst BP threshold, the gap between the BP and the MAP thresholds is big for this ensemble. Although its BP threshold improves significantly after applying spatial coupling with $m = 1$, the coupled threshold $\varepsilon^{1}_{\mathrm{SC}}$ is still much worse than those of the other cases. The SC-HCC-I ensemble has the best $\varepsilon^{1}_{\mathrm{SC}}$ between the considered SC-HCCs ensembles. Overall, however, the Type-II BCC ensemble still has the best $\varepsilon^{1}_{\mathrm{SC}}$ according to the results in Table III.

To make the comparison more complete, we consider SC-HCC ensembles of higher rates and higher coupling memories. In order to obtain higher rate R, we consider random puncturing with $\rho^{\mathrm{U}} = 0$, $\rho^{\mathrm{L}} = 0$ and $\rho_2 = \rho^{\mathrm{I}} = \frac{1-R}{2R}$.[2] The obtained BP and MAP thresholds are summarized in Table IV. The corresponding BP thresholds for Type-II BCCs in [4] are also given in this table. As we discussed, Type-II BCCs yield better thresholds than Type-I BCCs. Therefore, only the thresholds of Type-II BCCs are reported in Table IV.

According to the results in the table, for all rates the HCC ensembles suffer from poor BP thresholds and among them, the HCC-II ensemble has the poorest BP threshold. The MAP thresholds of the HCC ensembles are almost identical and very close to the Shannon limit for all rates. However, for some rates, the HCC-III ensemble has worse MAP threshold than those of the two other HCC ensembles. However, this threshold is still slightly better than the MAP threshold of the BCC ensemble.

The BP thresholds of the spatially coupled ensembles with coupling memory $m = 1, 3, 5$ are presented in the columns corresponding to $\varepsilon^{1}_{\mathrm{SC}}$, $\varepsilon^{3}_{\mathrm{SC}}$ and $\varepsilon^{5}_{\mathrm{SC}}$, respectively. In all considered cases of SC-HCCs, the BP thresholds improve by increasing the coupling memory. For a large enough coupling memory, the BP thresholds achieve the threshold of the MAP decoder. It can be seen that, for a fixed coupling memory, the Type-II SC-HCC ensembles yield better BP thresholds than the corresponding Type-I SC-HCC ensembles and for them saturation occurs for smaller m. Although the Type-II BCC ensemble has the best BP threshold for $m = 1$ for all rates, by increasing m the BP thresholds of the SC-HCC ensembles get better than those of BCCs.

VII. CONCLUSIONS

In this paper, we have investigated the impact of spatial coupling on the BP thresholds of HCCs. Similarly to BCCs, these codes are a powerful class of turbo-like codes and their MAP thresholds are even better than those of BCCs. We have shown that the BP thresholds of the HCC ensembles improve significantly by applying spatial coupling and threshold saturation occurs. By selecting the component encoders properly,

[2] To have consistent notation with [4], we replace ρ^{I} with ρ_2 in the table.

TABLE IV
THRESHOLDS FOR PUNCTURED BCCS AND HCCS

Ensemble	Type	Rate	ρ_2	ε_{BP}	ε_{MAP}	$\varepsilon_{\text{SC}}^{1}$	$\varepsilon_{\text{SC}}^{3}$	$\varepsilon_{\text{SC}}^{5}$
BCC	Type-II	$1/3$	1.0	0.5541	0.6653	0.6651	0.6653	0.6653
HCC-I	Type-I	$1/3$	1.0	0.4961	0.6666	0.6398	0.6621	0.6651
HCC-I	Type-II	$1/3$	1.0	0.4961	0.6666	0.6611	0.6666	0.6666
HCC-II	Type-I	$1/3$	1.0	0.3480	0.6666	0.5667	0.6166	0.6312
HCC-II	Type-II	$1/3$	1.0	0.3480	0.6666	0.6181	0.6652	0.6666
HCC-III	Type-I	$1/3$	1.0	0.5456	0.6665	0.5943	0.6243	0.6352
HCC-III	Type-II	$1/3$	1.0	0.5456	0.6665	0.6382	0.6655	0.6663
BCC	Type-II	$1/2$	0.5	0.3013	0.4993	0.4988	0.4993	0.4993
HCC-I	Type-I	$1/2$	0.5	0.2486	0.4999	0.4601	0.4947	0.4982
HCC-I	Type-II	$1/2$	0.5	0.2486	0.4999	0.4846	0.4999	0.4999
HCC-II	Type-I	$1/2$	0.5	0.1502	0.4999	0.3766	0.4472	0.4659
HCC-II	Type-II	$1/2$	0.5	0.1502	0.4999	0.4272	0.4970	0.4999
HCC-III	Type-I	$1/2$	0.5	0.3501	0.4999	0.4135	0.4540	0.4685
HCC-III	Type-II	$1/2$	0.5	0.3501	0.4999	0.4597	0.4979	0.4994
BCC	Type-II	$2/3$	0.25	–	0.3331	0.3323	0.3331	0.3331
HCC-I	Type-I	$2/3$	0.25	0.0622	0.3333	0.2671	0.3274	0.3314
HCC-I	Type-II	$2/3$	0.25	0.0622	0.3333	0.2952	0.3327	0.3333
HCC-II	Type-I	$2/3$	0.25	0.0331	0.3333	0.1972	0.2787	0.3024
HCC-II	Type-II	$2/3$	0.25	0.0331	0.3333	0.2355	0.3252	0.3328
HCC-III	Type-I	$2/3$	0.25	0.1820	0.3332	0.2434	0.2876	0.3044
HCC-III	Type-II	$2/3$	0.25	0.1820	0.3332	0.2821	0.3295	0.3327
BCC	Type-II	$3/4$	0.166	–	0.2491	0.2481	0.2491	0.2491
HCC-I	Type-I	$3/4$	0.166	0.0199	0.2499	0.1662	0.2398	0.2481
HCC-I	Type-II	$3/4$	0.166	0.0199	0.2499	0.1930	0.2479	0.2499
HCC-II	Type-I	$3/4$	0.166	0.0102	0.2492	0.1161	0.1919	0.2184
HCC-II	Type-II	$3/4$	0.166	0.0102	0.2492	0.1431	0.2348	0.2477
HCC-III	Type-I	$3/4$	0.166	0.1106	0.2491	0.1624	0.2043	0.2215
HCC-III	Type-II	$3/4$	0.166	0.1106	0.2491	0.1933	0.2433	0.2485
BCC	Type-II	$4/5$	0.125	–	0.1999	0.1986	0.1999	0.1999
HCC-I	Type-I	$4/5$	0.125	0.0085	0.1999	0.1091	0.1821	0.1982
HCC-I	Type-II	$4/5$	0.125	0.0085	0.1999	0.1315	0.1956	0.1997
HCC-II	Type-I	$4/5$	0.125	0.0043	0.1999	0.0747	0.1406	0.1677
HCC-II	Type-II	$4/5$	0.125	0.0043	0.1999	0.0940	0.1795	0.1970
HCC-III	Type-I	$4/5$	0.125	0.0743	0.1999	0.1173	0.1557	0.1726
HCC-III	Type-II	$4/5$	0.125	0.0743	0.1999	0.1422	0.1917	0.1990
BCC	Type-II	$9/10$	0.055	–	0.0990	0.0954	0.0990	0.0990
HCC-I	Type-I	$9/10$	0.055	0.0006	0.0999	0.0245	0.0603	0.0822
HCC-I	Type-II	$9/10$	0.055	0.0006	0.0999	0.0317	0.0798	0.0960
HCC-II	Type-I	$9/10$	0.055	0.0003	0.0990	0.0159	0.0427	0.0610
HCC-II	Type-II	$9/10$	0.055	0.0003	0.0990	0.0208	0.0617	0.0850
HCC-III	Type-I	$9/10$	0.055	0.0190	0.0990	0.0367	0.0587	0.0714
HCC-III	Type-II	$9/10$	0.055	0.0190	0.0990	0.0463	0.0805	0.0941

we can optimize the HCC ensemble for higher BP or MAP thresholds. However, optimizing the HCC ensemble for higher BP or MAP threshold does not guarantee a high BP threshold for SC-HCC for a fixed coupling memory.

REFERENCES

[1] A. Jiménez Feltström and K.Sh. Zigangirov, "Periodic time-varying convolutional codes with low-density parity-check matrices," *IEEE Trans. Inf. Theory*, vol. 45, no. 5, pp. 2181–2190, Sep. 1999.

[2] S. Kudekar, T.J. Richardson, and R.L. Urbanke, "Threshold saturation via spatial coupling: Why convolutional LDPC ensembles perform so well over the BEC," *IEEE Trans. Inf. Theory*, vol. 57, no. 2, pp. 803 –834, Feb. 2011.

[3] S. Moloudi, M. Lentmaier, and A. Graell i Amat, "Spatially coupled turbo codes," in *Proc. 8th Int. Symp. on Turbo Codes and Iterative Inform. Process. (ISTC)*, Bremen, Germany, 2014.

[4] S. Moloudi, M. Lentmaier, and A. Graell i Amat, "Spatially coupled turbo-liked codes," submitted to *IEEE Trans. Inf. Theory*, available online at https://arxiv.org/pdf/1604.07315v1.pdf, Dec. 2015.

[5] S. Moloudi, M. Lentmaier, and A. Graell i Amat, "Threshold saturation for spatially coupled turbo-like codes over the binary erasure channel," in *Inf. Theory Workshop (ITW)*, Jeju, South Korea, Oct 2015.

[6] S. Moloudi, M. Lentmaier, and A. Graell i Amat, "Finite Length Weight Enumerator Analysis of Braided Convolutional Codes," in *Proc. The Inter. Symp. on Inf. Theory and Its Applications (ISITA)*, Oct. 2016.

[7] E. Rosnes and A. Graell i Amat, "Performance analysis of 3-d turbo codes," *IEEE Trans. on Inf. Theory*, vol. 57, no. 6, pp. 3707–3720, June 2011.

[8] C. Koller, A. Graell i Amat, J. Kliewer, F. Vatta, and D. J. Costello, "Hybrid concatenated codes with asymptotically good distance growth," in *Proc. 5th Int. Symp. on Turbo Codes and Related Topics*, Sep. 2008.

[9] Cyril Méasson, *Conservation laws for coding*, Ph.D. thesis, École Polytechnique Fédérale de Lausanne, 2006.

[10] B.M. Kurkoski, P.H. Siegel, and J.K. Wolf, "Exact probability of erasure and a decoding algorithm for convolutional codes on the binary erasure channel," in *Proc. IEEE Global Telecommun. Conference (GLOBECOM)*, 2003.